

# **Kinematics of Molecular Hydrogen Emission from Pre-planetary Nebulae: RAFGL 2688 and RAFGL 618**

Joel H. Kastner<sup>1</sup>, David A. Weintraub<sup>2</sup>, Ian Gatley<sup>1</sup>, and LeeAnn Henn<sup>3</sup>

Received \_\_\_\_\_; accepted \_\_\_\_\_

---

<sup>1</sup>Chester F. Carlson Center for Imaging Science, Rochester Institute of Technology, 54 Lomb Memorial Dr., Rochester, NY 14623-5604 USA; jhk@cis.rit.edu

<sup>2</sup>Department of Physics & Astronomy, Vanderbilt University, P.O. Box 1807 Station B, Nashville, TN 37235

<sup>3</sup>Center for Space Research, Massachusetts Institute of Technology, NE80-6007, Cambridge, MA 02139 USA

## ABSTRACT

We present high spectral resolution maps of near-infrared molecular hydrogen emission from the bipolar pre-planetary nebulae RAFGL 2688 and RAFGL 618, obtained with the NOAO Phoenix spectrometer. The measured velocity gradients along the polar axes of both nebulae indicate that the highest velocity gas lies closest to the central stars. These results support the suggestion that the polar  $\text{H}_2$  emission regions of both nebulae contain shocked gas formed as fast ( $\sim 50 - 150 \text{ km s}^{-1}$ ), collimated, post-asymptotic giant branch (AGB) winds collide with slower-moving ( $\sim 10 - 20 \text{ km s}^{-1}$ ) material previously ejected while the central stars were still on the AGB. The kinematics of  $\text{H}_2$  emission perpendicular to the polar axis of RAFGL 2688 are consistent with a model combining expansion along the equator at  $5 - 10 \text{ km s}^{-1}$  with rotation about the polar axis at  $5 - 10 \text{ km s}^{-1}$ . The rapid onset of the common envelope phase of a close binary system may explain both the bipolar structure of RAFGL 2688 and the presence and complex kinematics of its shocked  $\text{H}_2$  emission.

*Subject headings:* pre-planetary nebulae: individual (RAFGL 2688, RAFGL 618) — pre-planetary nebulae: molecules — stars: mass loss — stars: AGB and post-AGB — ISM: dust

## 1. Introduction

The bulk of the mass lost by stars of initial mass  $\sim 1 - 8 M_{\odot}$  is shed while such stars are on the asymptotic giant branch (AGB). Evidence is fast accumulating that, during late AGB or post-AGB evolutionary stages, the mass loss geometry of such stars changes from more or less spherically symmetric to axially symmetric, with the result that the vast majority of planetary nebulae (PNs) — the endpoints of post-main sequence stellar evolution for intermediate-mass stars — exhibit axisymmetric structures, ranging from elliptical to bipolar (see, e.g., reviews compiled by Kastner, Soker, & Rappaport 2000). Planetaries in the latter structural category are very likely to possess molecular envelopes (presumably the remnants of the ejected AGB envelope) that are readily detectable in the near-infrared rovibrational lines of  $H_2$  (Kastner et al. 1996). The available data suggest, furthermore, that the onset of near-infrared  $H_2$  emission in PNs can be traced back to the pre-planetary nebula (PPN) phase but *not* back to the AGB phase of evolution (Weintraub et al. 1998). These observations suggest that further studies of  $H_2$  emission from PPNS and PNs may offer insight into the transition from AGB star to PN and from spherical to axisymmetric mass loss.

The Egg Nebula (RAFGL 2688; Ney et al. 1975) is perhaps the best-known example of such a transition object. Recent *Hubble Space Telescope* (HST) optical and near-infrared images of the Egg reveal a striking juxtaposition of circularly and axially symmetric structures (Sahai et al. 1998a, b). This puzzling combination of structures has been detected in HST images of several other PPNS and PNs (see, e.g., reviews compiled by Kastner, Soker, & Rappaport 2000). An outstanding feature of RAFGL 2688, however, is the “quadrupolar” morphology of  $2.122 \mu m$   $H_2$  emission detected in near-infrared images (Gatley et al. 1988); this structure is seen most clearly in an HST/NICMOS image (Fig. 1; Sahai et al. 1998a). This image shows that the linear extents and bow-shock-like structures of the polar and equatorial plane  $H_2$  emission regions are very similar, suggesting a common origin. Furthermore, the sharp, limb-brightened boundaries of the  $H_2$  emission in all four “lobes” is suggestive of a fairly sudden event in the object’s recent past.

The kinematics of molecular emission from RAFGL 2688 have been the subject of numerous

investigations. Bieging & Nguyen-Q-Rieu (1988, 1996) and Cox et al. (2000) mapped the velocity distribution of rotational emission of various species with radio interferometers, and Cox et al. (1997) imaged near-IR rovibrational  $H_2$  emission at moderate velocity resolution. Radio interferometric observations of HCN by Bieging & Nguyen-Q-Rieu yielded the rather surprising result of velocity gradients both along *and perpendicular to* the polar axis of the system, a result confirmed by Cox et al. These gradients, which are of similar magnitude, were interpreted by Bieging & Nguyen-Q-Rieu (1988, 1996) as arising out of a combination of spherical expansion and rotation about the polar axis. Cox et al. (1997, 2000) and Lucas et al. (2000), however, interpret the  $H_2$  kinematics of RAFGL 2688 in terms of a system of multiple jets.

The evolved bipolar nebula RAFGL 618 (Westbrook et al. 1975) might be considered the direct evolutionary descendent of RAFGL 2688 in many respects. Both objects display molecule-rich circumstellar envelopes, carbon-rich circumstellar chemistries, and dusty, bipolar reflection nebulosities. Whereas RAFGL 2688 harbors an F-type central star and is not known to contain an H II region, RAFGL 618 possesses a B-type central star and compact H II region, suggesting that the latter nebula has evolved farther toward the PN stage. Like the Egg Nebula, RAFGL 618 displays bright near-infrared  $H_2$  emission, but in the case of RAFGL 618 the  $H_2$  emission appears to be confined to a region along its polar axis (Latter et al. 1995).

While the “quadrupolar” structure of the  $H_2$  emission in the Egg appears to be unique, it may be a short-lived evolutionary phase common to many or most AGB stars as they go through the transition to PPNe. In RAFGL 618, however, the  $H_2$  morphology also is unusual as emission is found only along the polar axes, whereas most PPN in which  $H_2$  is detected exhibit the strongest  $H_2$  along the equatorial plane (Kastner et al. 1996). Thus, the kinematics and morphology of  $H_2$  emission from these two objects are strongly deserving of more careful study. To investigate the  $H_2$  velocity gradients of RAFGL 2688 in detail, we obtained a series of high-resolution, long-slit

spectra in the  $2.12 \mu\text{m}$  region with the NOAO<sup>4</sup> Phoenix near-infrared spectrometer (Hinkle et al. 1998). We also obtained a Phoenix spectrum of  $2.12 \mu\text{m}$   $\text{H}_2$  emission from RAFGL 618. As we now describe, examination and comparison of the  $\text{H}_2$  kinematics of these two objects, as revealed in the Phoenix spectroscopic data, offer clues to their detailed structures and recent evolutionary histories.

## 2. Observations

Data presented here were obtained with Phoenix on the 2.1 m telescope at Kitt Peak, AZ, in 1997 June (RAFGL 2688) and 1997 December (RAFGL 618). Phoenix illuminates a  $256 \times 1024$  section of an Aladdin InSb detector array. The spectrograph slit was  $\sim 60'' \times 1.4''$  oriented approximately east-west. The pixel scale along the dispersion axis of the spectrograph was  $1.29 \text{ km s}^{-1}$ . From the widths of OH airglow lines present in the raw spectra, we estimate the velocity resolution as  $\sim 4 \text{ km s}^{-1}$  at the time these spectra were obtained. This resolution is comparable to that of the mm-wave molecular line interferometry (e.g., Bieging & Nguyen-Q-Rieu 1996), and represents an order of magnitude improvement over previous imaging spectroscopy of  $\text{H}_2$  emission from RAFGL 2688 (Cox et al. 1997). The pixel scale in the cross-dispersion direction was  $0.35''$ , and the spatial resolution was  $\sim 1.5''$ .

A spectral image centered near the  $2.1218 \mu\text{m}$   $S(1), v = 1 - 0$  transition of  $\text{H}_2$  was obtained at each of 12 spatial positions as the slit was stepped from south to north across RAFGL 2688. The step size,  $1.0''$ , provided coverage of the entire  $\text{H}_2$  emitting region (Fig. 1) with spatial sampling approximating the slit height. For RAFGL 618, whose bright  $\text{H}_2$  emission regions are oriented almost perfectly east-west (Latter et al. 1995) — parallel to the Phoenix slit — we obtained a single spectral image centered on the object. Integration times for both sources were 1200 sec per position. Spectral images were reduced and wavelength calibrated as described by Weintraub et

---

<sup>4</sup>National Optical Astronomy Observatories is operated by Associated Universities for Research in Astronomy, Inc., for the National Science Foundation.

al. (1998). Bad pixels were removed by calculating the running mean for  $7 \times 7$  groups of pixels and replacing outliers in each pixel group with the running mean. For the RAFGL 2688 data, the reduced spectral images were stacked in declination according to the commanded telescope offsets, to produce a (RA, dec, velocity) data cube of  $\text{H}_2$  emission.

### 3. Results

#### 3.1. RAFGL 2688

##### 3.1.1. $\text{H}_2$ position-velocity maps and selected spectra

Calibrated spectral images of RAFGL 2688 are presented in Fig. 2. All four distinct  $\text{H}_2$  emitting regions (hereafter referred to as the N, E, S, and W lobes) seen in the NICMOS image (Fig. 1) are clearly detected in these spectral images (see, e.g., the dec =  $-1''$  panel). In addition, the large velocity gradients of molecular emission in RAFGL 2688 are readily apparent in the Phoenix data. The S lobe  $\text{H}_2$  emission (top 4 panels of Fig. 2) is predominantly redshifted with respect to the systemic velocity of RAFGL 2688 ( $V_{sys}$ ), with velocities ranging from  $\sim -5 \text{ km s}^{-1}$  to  $\sim +30 \text{ km s}^{-1}$  relative to  $V_{sys}$ . The N lobe emission (bottom 4 panels) appears almost as a “mirror image” of the S lobe in terms of its velocity pattern, with emission predominantly at blueshifted velocities ranging from  $\sim -35 \text{ km s}^{-1}$  to  $\sim +5 \text{ km s}^{-1}$  relative to  $V_{sys}$ . The velocity domains of the N and S lobes are well illustrated in representative spectra extracted from the images obtained at declination offsets of  $+4''$  and  $-4''$ , respectively (Fig. 3a).

As expected from the known position angle (PA) of the polar axis of the system, PA  $\sim 12^\circ$  (Weintraub et al. 2000), the E lobe is detected between declination offsets of  $-3''$  and  $+2''$ , whereas the W lobe emission is detected between offsets of  $-2''$  and  $+3''$ . The position-velocity images obtained at these positions dramatically demonstrate the E-W velocity gradient previously detected in molecular emission line studies of RAFGL 2688, as do representative spectra extracted from the E and W lobe emission regions in the spectral image obtained at  $0''$  declination offset

(Fig. 3b). That is, the E lobe is primarily blueshifted, whereas the W lobe is primarily redshifted. As we discuss in more detail below, however, the E-W and N-S velocity gradients differ in detail. In addition, the spectra in Fig. 3 illustrate that the  $H_2$  line profiles of the E and W lobes are generally narrower than those of the N and S lobes.

The Phoenix spectral images also reveal velocity structure *within* the N, S, and E lobes. In particular, the brightest emission from the S lobe is seen to migrate from lower to higher redshifted velocities moving inward (northward) from its tip at  $-5''$  in dec to  $-2''$  in dec. The N lobe exhibits precisely complementary behavior, with its brightest emission migrating from lower to higher blueshifted velocities moving inward (southward) from  $+6''$  in dec to  $+2''$  in dec. The E lobe also shifts in central velocity with declination offset, migrating from larger to smaller blueshifted velocities moving from south to north (i.e., from  $-3''$  to  $+2''$  in declination offset). In contrast, the velocity centroid of the W lobe does not shift noticeably with declination offset.

### 3.1.2. $H_2$ data cube and velocity centroids

In Fig. 4 we display selected velocity planes from the  $H_2$  data cube constructed for RAFGL 2688. The four principal “lobes” of  $H_2$  emission are apparent again, with one pair oriented parallel (roughly N-S) and one perpendicular (roughly E-W) to the polar axis. The velocity gradients in the N-S and E-W  $H_2$  lobe pairs are plainly evident in these images, with the N and E lobes blueshifted by up to  $\sim 25 \text{ km s}^{-1}$  and the S and W lobes similarly redshifted. As previously mentioned, however, the N-S and E-W  $H_2$  lobe pairs differ in their detailed kinematic signatures, as we now further describe.

The polar  $H_2$  lobes of RAFGL 2688 each display velocity gradients along the polar axis. This velocity gradient is apparent in the velocity-resolved images of RAFGL 2688 (Fig. 4). At the most extreme blueshifted and redshifted velocity intervals, respectively, only those portions of the N and S lobes nearest the inferred position of the central star are apparent, whereas the outer regions (tips) of the lobes appear brightest at more moderate radial velocities. This trend is made

more quantitative in a plot of the velocity centroid of H<sub>2</sub> emission as a function of position along the polar axis (Fig. 5). To construct this plot, we extracted spectra at each declination offset (see caption of Fig. 3). We then fit a Gaussian function to the H<sub>2</sub> line profile in each spectrum, to obtain the line velocity centroid. The resulting trend in the velocity centroids (Fig. 5) is easily anticipated based on the position-velocity images themselves (Fig. 2); i.e., relatively low velocity emission ( $\sim \pm 4 \text{ km s}^{-1}$ ) is seen at the tips of the lobes, while the highest velocity emission in each lobe ( $\sim \pm 30 \text{ km s}^{-1}$ ) is found nearest the position of the central star. This trend is remarkably similar to that observed in the position-velocity image of RAFGL 618 (§3.2).

In contrast, images extracted from the data cube (Fig. 4) demonstrate that the E lobe displays a gradient from north to south, *perpendicular* to the line joining it to the central star’s position. Specifically, note that in the image centered at  $-26.6 \text{ km s}^{-1}$ , only the southernmost tip of the E lobe appears, whereas in the image centered at  $-0.7 \text{ km s}^{-1}$ , the entire E lobe is present. Hence, the Phoenix data appear to resolve kinematically the distinct emission components of the E lobe that are resolved spatially in the NICMOS H<sub>2</sub> image of RAFGL 2688 (Fig. 1). The W lobe, meanwhile, does not reveal similar velocity structure, a result qualitatively consistent with its more localized appearance in the NICMOS image.

### 3.2. RAFGL 618

The Phoenix spectral image obtained for RAFGL 618 is displayed in Fig. 6. Bright H<sub>2</sub> emission is detected along the entire polar axis of RAFGL 618. Spectra extracted from this image (Fig. 7) demonstrate that very high velocity H<sub>2</sub> emission (up to  $\sim \pm 120 \text{ km s}^{-1}$  in each lobe) is present in this bipolar outflow. Similarly broad line wings have been detected previously in millimeter- and submillimeter-wave molecular spectra of RAFGL 618 (e.g., Gammie et al. 1989; Neri et al. 1992; Meixner et al. 1998). The H<sub>2</sub> spectra demonstrate unequivocally that — as is the case for RAFGL 2688 — the highest velocity molecular material is found closest to the central star of RAFGL 618. A similar result was inferred for RAFGL 618 by Gammie et al., based on the relative strengths of line wing emission in single-dish CO (2-1) and CO (3-2) spectra.

## 4. Discussion

### 4.1. A kinematical model of H<sub>2</sub> emission from RAFGL 2688

We now construct a detailed, empirical model of the H<sub>2</sub> kinematics of RAFGL 2688. In formulating this model, we are guided by our observations that (1) the polar lobes are characterized by velocity gradients in which the fastest moving material is found closest to the star, and the slowest moving material is found at the tips of the H<sub>2</sub> emission regions; and (2) the H<sub>2</sub> emission seen projected along the equatorial plane contains a substantial velocity gradient east to west and a second, smaller velocity gradient in the E lobe that runs north to south.

#### 4.1.1. Polar lobe H<sub>2</sub> kinematics

The Gaussian shapes of the spatially integrated H<sub>2</sub> emission line profiles of the polar lobes of RAFGL 2688 (Fig. 3a) are similar to the molecular emission line profiles detected in the radio regime from species such as CO and HCN (e.g., Bieging & Nguyen-Q-Rieu 1996). The H<sub>2</sub> line profiles can be understood in the context of the detailed morphology of H<sub>2</sub> emission seen in the NICMOS image (Fig. 1). In this image the N and S lobes appear as limb-brightened cavities. The emission peaks of the line profiles correspond to the brightest regions of the lobes — their limbs (i.e., outlines) — whereas the line wings are produced by emission from within the fainter lobe interiors, which is dominated by material in the near sides (blue wings) and far sides (red wings) of the lobes.

The peak of the line profile therefore indicates the line of sight component of the H<sub>2</sub> velocity at the lobe limb, and we can infer the deprojected N and S lobe H<sub>2</sub> velocities as a function of position given an estimate of  $i$ , the inclination of the polar axis of the system out of the plane of the sky. Previous results (Yusef-Zadeh et al. 1984; Sahai et al. 1998a) suggest  $i \sim 15^\circ$ . The velocities we measure at the tips of the lobes ( $\sim 5 \text{ km s}^{-1}$ ; Fig. 5) then suggest that the gas in this region is expanding away from the central star at a velocity  $\sim 20 \text{ km s}^{-1}$ . We further infer that

the H<sub>2</sub> velocities in the regions of the lobes within  $\sim 1''$  of the inferred position of the central star rise to  $\sim 70$  km s<sup>-1</sup>.

For simplicity, we assume this behavior can be described by an inverse power law of the form

$$v(\Delta\alpha, \Delta\delta) = v_0 \left(\frac{r_0}{r}\right)^p \sin i \quad (1)$$

for (RA, dec) offsets  $(\Delta\alpha, \Delta\delta)$  that lie within 45° of the projected polar axis of RAFGL 2688, where  $v_0$  is the velocity at the tips of the polar lobes,  $v(\Delta\alpha, \Delta\delta)$  is the observed radial velocity at projected angular radius  $r = ((\Delta\alpha)^2 + (\Delta\delta)^2)^{1/2}$  from the central star, and  $i$  is the inclination of the polar axis out of the plane of the sky. Based on the foregoing discussion of line profiles, we make the further simplification that the polar H<sub>2</sub> emission is dominated by emission from the lobe limbs.

#### 4.1.2. Equatorial plane H<sub>2</sub> kinematics

*If one postulates that all of the east-west H<sub>2</sub> emission is confined to a narrow region along the equatorial plane, then a component of azimuthal velocity must be present in the material responsible for this emission. Such a structure might be analogous to that of the equatorial “skirt” observed in  $\eta$  Car (Smith, Gehrz, & Krautter 1998). Although the kinematics of the two objects appear to differ in detail (Zethson et al. 1999), the H<sub>2</sub> morphology in the NICMOS image (Fig. 1) is consistent with the confinement of the H<sub>2</sub>-emitting material in RAFGL 2688 to the plane of the system: knot E2 is brighter than knot E4, as expected if the former is directed toward the observer and the latter is directed away from the observer; while E1 and E3, which mark the perpendiculars to the polar axis (see Weintraub et al. 2000, their Fig. 6), are of similar intensity, as expected if we view these structures through similar columns of intervening material.*

We therefore assume that the equatorial plane H<sub>2</sub> kinematics consist of a combination of azimuthal (rotation) and radial (expansion) velocity components. We calculate these velocities from the relation

$$v(\Delta\alpha, \Delta\delta) = (v_e \sin \phi + v_r \cos \phi) \cos i \quad (2)$$

for (RA, dec) offsets  $(\Delta\alpha, \Delta\delta)$  that lie within  $45^\circ$  of the projected equatorial plane of RAFGL 2688, where  $v_e$  is the expansion velocity,  $v_r$  is the rotational velocity about the polar axis, and  $\phi$  is the azimuthal angle with respect to the polar axis of RAFGL 2688, given by

$$\phi = \tan^{-1} \left( \frac{\Delta x}{\Delta y \sin i} \right). \quad (3)$$

Offsets  $(\Delta x, \Delta y)$  are then related to  $(\Delta\alpha, \Delta\delta)$  via a rotation of the coordinate system by the projected position angle of the polar axis on the plane of the sky.

#### 4.1.3. Comparison with data

Model parameters  $v_0$  and  $p$  are relatively well constrained by Fig. 5, from which we infer  $v_0 \sim 20 \text{ km s}^{-1}$  and  $p \sim 0.7$ . It is more difficult to constrain the values of the parameters governing the equatorial plane H<sub>2</sub> radial velocities,  $v_e$  and  $v_r$ . To do so, we compared model velocity field images ( $v(\Delta\alpha, \Delta\delta)$ ) calculated for a range of values of  $v_e$  and  $v_r$  with velocity centroids calculated from the Phoenix data cube (see, e.g., Bieging & Rieu 1996). We find qualitative and rough quantitative agreement between model and data for values of both  $v_e$  and  $v_r$  in the range  $5 - 10 \text{ km s}^{-1}$ , with the additional constraint  $v_e + v_r \sim 15 \text{ km s}^{-1}$ . An example of the results for a representative successful model is displayed in Fig. 8. In this figure the model velocity centroid image is calculated from Eqs. 1 and 2 for values of  $v_e = 5 \text{ km s}^{-1}$  and  $v_r = 10 \text{ km s}^{-1}$ . There is clear qualitative agreement between the model and observed velocity images for these parameter values, in the sense that the overall distribution of redshifted and blueshifted emission is captured by the model. Furthermore, this model reproduces the important details of the observed H<sub>2</sub> velocity distribution previously described. Specifically, the model recovers the magnitudes and positions of the observed blueshifted velocity extrema near (RA,dec) offsets  $(+1'', +2'')$  in the N lobe and  $(+5'', -3'')$  in the E lobe, as well as the magnitudes and positions of redshifted velocity extrema near offsets  $(-1'', -2'')$  in the S lobe and at  $(-4'', +3'')$  in the W lobe.

Empirically, we find these parameter values —  $v_0 = 20 \text{ km s}^{-1}$ ,  $p = 0.7$ ,  $v_e = 5 - 10 \text{ km s}^{-1}$ , and  $v_r = 5 - 10 \text{ km s}^{-1}$  — provide the best agreement between model and data in terms of

overall qualitative appearance of the velocity images as well as in the location *and* magnitude of the velocity extrema. However, this model cannot be considered a “best fit” to the data. Rather, the foregoing comparison of calculated and observed velocity fields offers an indication of the magnitude of an azimuthal velocity component relative to the components of radial expansion both parallel and perpendicular to the polar axis.

#### 4.2. Alternative models

The kinematic model described in §4.1 is not unique. For example, on the basis of high spatial and spectral resolution CO maps, which display kinematics very similar to those seen in H<sub>2</sub> emission, Cox et al. (1997, 2000) and Lucas et al. (2000) have proposed that the velocity gradients parallel and perpendicular to the polar axis result from a multipolar system of jets whose directions of motion are everywhere directed *radially outward* from the central star. Since the entire fan-like eastern H<sub>2</sub> emission region is blueshifted, the Cox et al. model requires that these outflows must be directed well “above” the equatorial plane of the system, toward the observer, while the outflows responsible for the western H<sub>2</sub> emission region are more tightly confined and directed “below” the equatorial plane, away from the observer. Hence, in this model, the remarkable orthogonality of the H<sub>2</sub> and CO emission morphologies is purely a result of viewing angle. Multiple symmetry axes are also suggested by observations of radio continuum emission (Jura et al. 2000). Chaotic precession of bipolar jets might explain these observations (see, e.g., Livio 2000 and references therein). The very similar linear extents of the orthogonal N-S and E-W molecular emission regions appear to pose a problem for any model invoking precessing jets, however.

Bieging & Nguyen-Q-Rieu (1988, 1996) have proposed a model in which the radio molecular line emission from the projected equatorial plane of RAFGL 2688 originates in an expanding, rotating equatorial disk or torus. Though qualitatively similar to the model proposed in §4.1, our model does not require that the H<sub>2</sub> emission arises from a disk. Rather, the E-W H<sub>2</sub> lobes, like the polar (N-S) H<sub>2</sub> lobes (see below), trace the interaction between material ejected along

the equatorial plane at two different epochs; indeed, the interferometric radio molecular line observations indicate that the molecular jets detected in CO may be responsible for shocks that produce the H<sub>2</sub> emission, based on the striking correspondence between the CO and H<sub>2</sub> emission morphologies (Lucas et al. 2000). There is no particular reason to assume that the previously ejected material forms a complete torus around the star and, indeed, Cox et al. (2000) and Morris & Sahai (2000) have argued, on the basis of radio and mid-infrared imaging, respectively, that no such structure exists. However, the optical and infrared morphology of the nebula — in particular, the apparent occultation of the southern H<sub>2</sub> lobe and reflection nebulosity within  $\sim 2''$  of the central star — does suggest the presence of a large ( $\sim 5''$  radius), optically thick structure.

### 4.3. Origin of the shocked H<sub>2</sub> emission

#### 4.3.1. The transition from spherical to axial symmetry

As noted by Sahai et al. (1998a), the detailed morphology of near-IR H<sub>2</sub> emission from RAFGL 2688 strongly supports previous suggestions that the emission arises in shocks formed by the interaction of recently-developed, fast-moving winds with slower-moving material. This relatively slow-moving material likely was ejected during the AGB phase of the progenitor star. Assuming J shocks are the origin of the gas heating that leads to H<sub>2</sub> emission then, according to model calculations (e.g., Burton, Hollenbach, & Tielens 1992), the shock fronts at the H<sub>2</sub> lobe tips are moving at a minimum velocity  $v_s \sim 10 \text{ km s}^{-1}$  in the frame of the preshocked (AGB) wind. This limit corresponds roughly to the energy threshold for excitation of the  $v = 1 - 0$   $S(1)$  H<sub>2</sub> line. Hence, if the velocities inferred for the tips of the polar lobes and for the equatorial region,  $\sim 20 \text{ km s}^{-1}$  and  $\sim 15 \text{ km s}^{-1}$ , respectively, consist of a superposition of (minimum) shock and AGB wind velocities, we infer that the AGB wind was ejected at  $v_{\text{AGB}} \sim 5 - 10 \text{ km s}^{-1}$ , which is typical of *low-mass* carbon stars. On the other hand, the nascent bipolar structure and strong H<sub>2</sub> emission of RAFGL 2688 hint at a relatively massive progenitor (Kastner et al. 1996) which may, in turn, suggest a larger AGB outflow velocity ( $v_{\text{AGB}} \sim 20 \text{ km s}^{-1}$ ; e.g., Kastner et al. 1993). If so,

it would appear that, at their leading edges, the shocks which excite H<sub>2</sub> have imparted very little momentum to the former AGB wind. In either case it is apparent that, well behind the leading edges of the shocks that excite the H<sub>2</sub> in the polar lobes, considerable wind acceleration has taken place. The maximum speed for non-dissociative shocks is  $\sim 25$  km s<sup>-1</sup> (Burton et al. 1992). Thus, within  $\sim 1''$  ( $\sim 1000$  AU) of the central star of RAFGL 2688, the outflow velocity of the gas is at least  $\sim 45$  km s<sup>-1</sup>, which is much larger than the outflow velocities of AGB stars. In RAFGL 618, meanwhile, the inferred polar outflow velocities very near the central star are at least  $\sim 100$  km s<sup>-1</sup> (neglecting projection effects), assuming the shocks are traveling at  $\sim 25$  km s<sup>-1</sup>.

We conclude that the velocity gradients along the polar axes of both RAFGL 2688 and RAFGL 618 trace rapid transitions from the “slow,” spherically symmetric winds of their AGB progenitors to faster, collimated, post-AGB winds. A likely mechanism for such a transition is that late AGB and post-AGB ejecta relatively close to the central star are accelerated with increasing efficiency as the star is “unveiled” and circumstellar material is exposed to a progressively hotter photosphere and, potentially, a stronger stellar magnetic field. Indeed, RAFGL 2688 has been observed to be increasing steadily in optical magnitude (Gottlieb & Liller 1976). These conditions would appear to be conducive to the formation of H<sub>2</sub> shocks during the post-AGB but pre-planetary nebula phase of bipolar nebulae, a scenario consistent with the conclusions of Weintraub et al. (1998). Such shocks could then play a central role in the transition from spherically symmetric to axisymmetric outflow, as the “young,” fast (but still predominantly molecular) wind driven by the emerging post-AGB star excavates bipolar cavities within the previously ejected red giant wind. The displacement from the central star to the tips of the H<sub>2</sub> lobes ( $\sim 6000$  AU), combined with the deprojected velocities at the lobe tips,  $v_0 \sim 20$  km s<sup>-1</sup>, suggests the H<sub>2</sub> lobes have a dynamical age of 1500 yr, which then serves as an upper limit to the post-AGB “unveiling” of the central star.

#### 4.3.2. The Egg Nebula as endpoint of common envelope binary evolution

A presently popular theory accounts for the structure of bipolar planetary nebulae as due to the interaction of a close binary system, in which the secondary diverts mass loss from and/or spins up the envelope of the primary (e.g., Soker 1997, 1998). According to a specific formulation of the binary progenitor model (Soker 1998), the relatively massive progenitors of bipolar PNs undergo a phase during the AGB evolution of the primary in which the secondary resides just outside the envelope of the primary and diverts mass loss into the equatorial plane. This phase is followed by a short-lived common envelope phase that, presumably, rapidly spins up the envelope of the primary; the carbon star V Hya, which displays  $V \sin i \sim 13 \text{ km s}^{-1}$ , may be undergoing such a phase at present (Barnbaum et al. 1995).

Many, though certainly not all, of the observed characteristics of RAFGL 2688 appear to be explained by such a model. Specifically, its notorious system of concentric broken arcs would result from episodic, spherically symmetric mass loss during a prolonged period of quasi-single star AGB mass loss preceding the common envelope phase; the subsequent formation of bipolar structure would be the result of the increasingly close proximity of a companion during the late AGB evolution of the primary; and the H<sub>2</sub> shocks would mark the rapid termination of a common envelope phase and the resultant sudden ejection of the remaining AGB star envelope. Hence, the H<sub>2</sub> emission regions are produced by bullet-like ejecta that have collided with material that was recently ejected — much of it along the equatorial plane — during the close binary phase preceding common envelope formation.

It would appear that no existing model can explain satisfactorily the rich phenomenology of the Egg Nebula. The molecular kinematics of its equatorial region remain particularly problematic for present models, whether or not a component of azimuthal velocity is present along the equatorial plane of the system. A pure radial outflow model cannot explain the striking orthogonality of the molecular emission from RAFGL 2688; furthermore, such a model is, at present, reliant on *ad hoc* physical mechanisms for the presence of multiple symmetry axes (e.g., Frank 2000). On the other hand, the azimuthal velocities of the equatorial H<sub>2</sub> emission suggested

by our model and the models of Bieging & Nguyen-Q-Rieu (1988, 1996) are far too large to be explained by Keplerian rotation; an alternative source of angular momentum is required. As proposed by Bieging & Nguyen-Q-Rieu, this angular momentum might be provided by magnetic fields that are corotating with the star. It is of considerable importance to establish whether sufficiently large fields can be generated via interaction with a close companion star (Bieging & Nguyen-Q-Rieu 1988, 1996) or by dynamo activity in the primary post-AGB star itself (e.g., Soker 2000; Blackman, Frank, & Welch 2000). The latter mechanism could be particularly effective if the central star has just undergone a common envelope phase, such that highly magnetically active interior layers of the star drive the molecular jets seen in CO and H<sub>2</sub>.

Support for this research was provided in part by a JPL/ISO grant to R.I.T. We acknowledge enlightening discussions with Adam Frank and Robert Lucas, and the helpful comments of the referee.

## REFERENCES

Barnbaum, C., Morris, M., & Kahane, C. 1995, *ApJ*, 450, 862

Bieging, J., & Nguyen-Q-Rieu 1988, *ApJ*, 324, 516

Bieging, J., & Nguyen-Q-Rieu 1996, *AJ*, 112, 706

Blackman, E., Frank, A., & Welch, C. 2000, *ApJ*, submitted (astro-ph/0005288)

Burton, M.G., Hollenbach, D.J., & Tielens, A.G.G.M. 1992, *ApJ*, 399, 563

Cox, P., et al. 1997, *A&A*, 321, 907

Cox, P., Lucas, R., Huggins, P.J., Forveille, T., Bachiller, R., Guilloteau, S., Mallard, J.P., & Omont, A. 2000, *A&A*, 353, L25

Frank, A. 2000, in “Asymmetrical Planetary Nebulae II: From Origins to Microstructures,” eds. J.H. Kastner, N. Soker, & S.A. Rappaport, *ASP Conf. Series*, Vol. 199, p. 225

Gammie, C., Knapp, G. R., Young, K., Phillips, T. G., Falgarone, E. 1989, *ApJ*, 345, L87

Garcia-Segura, G., Langer, N., Rozyczka, M., & Franco, J. 1999, *ApJ* 517, 767

Gatley, I., Depoy, D. L., & Fowler, A. M. 1988, *Science*, 242, 1264

Gottlieb, E.W., & Liller, W. 1976, *ApJ*, 207, L135

Hinkle, K. H., Cuberly, R., Gaughan, N., Heynssens, J., Joyce, R., Ridgway, S., Schmitt, P., & Simmons, J. E. 1998, *Proceedings of S.P.I.E.* 3354, 810

Jura, M., Turner, J.L., Van Dyk, S., & Knapp, G. 2000, *ApJ*, 528, L105

Kastner, J.H., Forveille, T., Zuckerman, B., & Omont, A. 1993, *A&A*, 275, 163

Kastner, J.H., Weintraub, D.A., Gatley, I., Merrill, K.M., & Probst, R.P. 1996, *ApJ*, 462, 777

Kastner, J.H., Soker, N., & Rappaport, S.A., eds. 2000, “Asymmetrical Planetary Nebulae II: From Origins to Microstructures,” ASP Conf. Series, Vol. 199

Latter, W. B., Kelly, D. M., Hora, J. L., Deutsch, L. K. 1995, ApJS, 100, 159

Livio, M. 2000, in “Asymmetrical Planetary Nebulae II: From Origins to Microstructures,” eds. J.H. Kastner, N. Soker, & S.A. Rappaport, ASP Conf. Series, Vol. 199, p. 243

Lucas, R., Cox, P., & Huggins, P.J. 2000, in “Asymmetrical Planetary Nebulae II: From Origins to Microstructures,” eds. J.H. Kastner, N. Soker, & S.A. Rappaport, ASP Conf. Series, Vol. 199, p. 285

Meixner, M., Campbell, M.T., Welch, W.J., & Likkel, L. 1998, ApJ, 509, 392

Morris, M., & Sahai, R. 2000, in “Asymmetrical Planetary Nebulae II: From Origins to Microstructures,” eds. J.H. Kastner, N. Soker, & S.A. Rappaport, ASP Conf. Series, Vol. 199, p. 143

Neri, R., Garcia-Burillo, S., Guelin, M., Cernicharo, J., Guilloteau, S., & Lucas, R. 1992, A&A, 262, 544

Ney, E. P., Merrill, K. M., Becklin, E. E., Neugebauer, G., & Wynn-Williams, C. G. 1975, ApJ, 198, L129

Sahai, R., Hines, D., Kastner, J.H., Weintraub, D.A., Trauger, J.T., Rieke, M.J., Thompson, R.I., & Schneider, G. 1998a, ApJ, 492, 163L

Sahai, R., et al. 1998b, ApJ, 493, 301

Skinner, C.J., et al. 1997, A&A, 328, 290

Smith, N., Gehrz, R. D., & Krautter, J. 1998, AJ, 116, 1332

Soker, N. 1997, ApJS, 112, 487

Soker, N. 1998, ApJ, 496, 833

Soker, N. 2000, in “Asymmetrical Planetary Nebulae II: From Origins to Microstructures,” eds. J.H. Kastner, N. Soker, & S.A. Rappaport, ASP Conf. Series, Vol. 199, p. 71

Su, K.Y.L., Volk, K., Kwok, S., & Hrivnak, B. 1998, ApJ, 508, 744

Weintraub, D.A., Huard, T., Kastner, J.H., & Gatley, I. 1998, ApJ, 509, 728

Weintraub, D.A., Kastner, J.H., Sahai, R., & Hines, D. 2000, ApJ, 531, 401

Westbrook, W.E., Becklin, E. E., Merrill, K. M., Neugebauer, G., Schmidt, M., Willner, S. P., & Wynn-Williams, C. G. 1975, ApJ, 202, 407

Yusef-Zadeh, F., Morris, M., & White, R.L. 1984, ApJ, 278, 186

Zethson, T., Johansson, S., Davidson, K., Humphreys, R.M., Ishabashi, K., & Ebbets, D. 1999, A&A, 344, 211

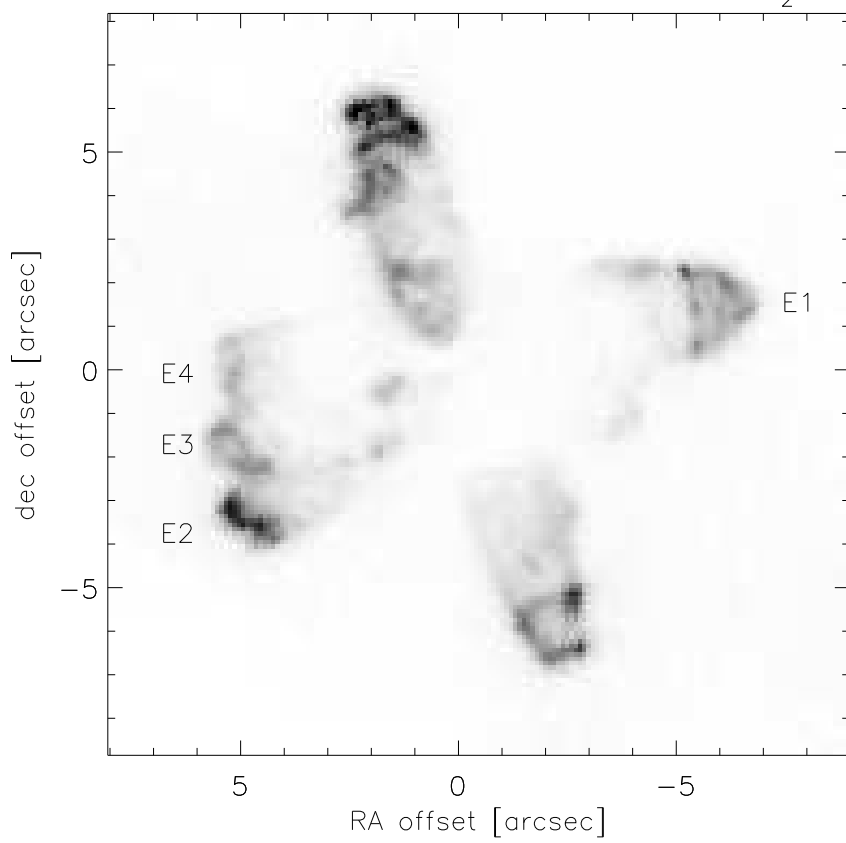
### Figure captions

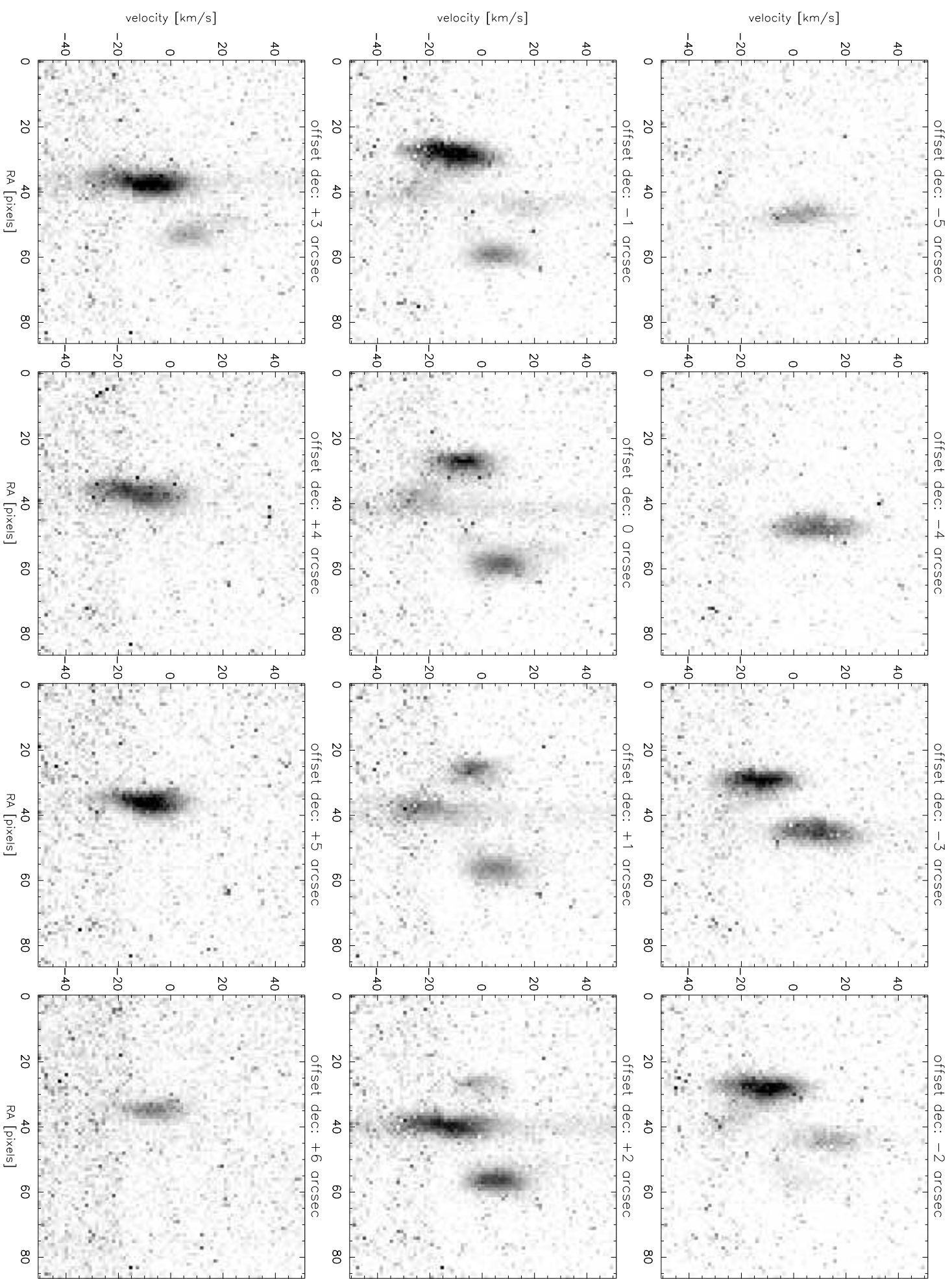
1. HST/NICMOS image of  $2.12 \mu\text{m}$   $\text{H}_2$  emission from RAFGL 2688 (Sahai et al. 1998a). Features identified E1–E4 by Sahai et al. are indicated.
2. Phoenix spectral images of RAFGL 2688. Images were obtained at the declination offsets indicated above each frame. Each calibrated image is represented as a position-velocity map, with RA running along image columns and radial velocity running along image rows. The velocity scale of each image is centered on the systemic velocity of RAFGL 2688 with respect to the local standard of rest,  $V_{sys} = -34 \text{ km s}^{-1}$  (e.g., Bieging & Nguyen-Q-Rieu 1996). East is to the left; the spatial scale is  $0.35''$  per pixel, with the central star located very near pixel column 42 (nebular continuum emission is also evident in the images in the center panels). Relative intensities in these and other images presented in this paper are represented with a linear greyscale unless otherwise indicated.
3. Spectra extracted *a*) from spectral images obtained at declination offsets of  $+4''$  (N lobe) and  $-4''$  (S lobe) and *b*) from spectral images obtained at  $0''$  declination offset (E and W lobes). Each spectrum is obtained by summing image sections of width  $4.5''$  in RA centered on the peak of  $\text{H}_2$  emission. The velocity scale of each spectrum is centered on the systemic velocity of RAFGL 2688 with respect to the local standard of rest.
4. Velocity-integrated  $\text{H}_2$  images of RAFGL 2688, extracted from the Phoenix data cube. Row and column image scales indicate offsets (arcsec) in RA and dec, respectively. Each image is integrated over  $\sim 5 \text{ km s}^{-1}$  and is centered at the velocity indicated. These velocities are relative to the systemic velocity of RAFGL 2688.
5. Radial velocity centroid, with respect to systemic velocity, of  $\text{H}_2$  emission vs. position along the polar axis of RAFGL 2688. Uncertainties in determinations of velocity centroids are approximately the symbol size.
6. Calibrated Phoenix spectral image of RAFGL 618. The velocity scale of the image is centered on the systemic velocity of RAFGL 618. East is to the left; the spatial scale is

$0.35''$  per pixel, with the central star located very near pixel column 18 (continuum emission is present at this position in the form of vertical band across the image). The image is displayed in a logarithmic greyscale to bring out the faint line wing emission, which extends to  $\sim \pm 120 \text{ km s}^{-1}$ .

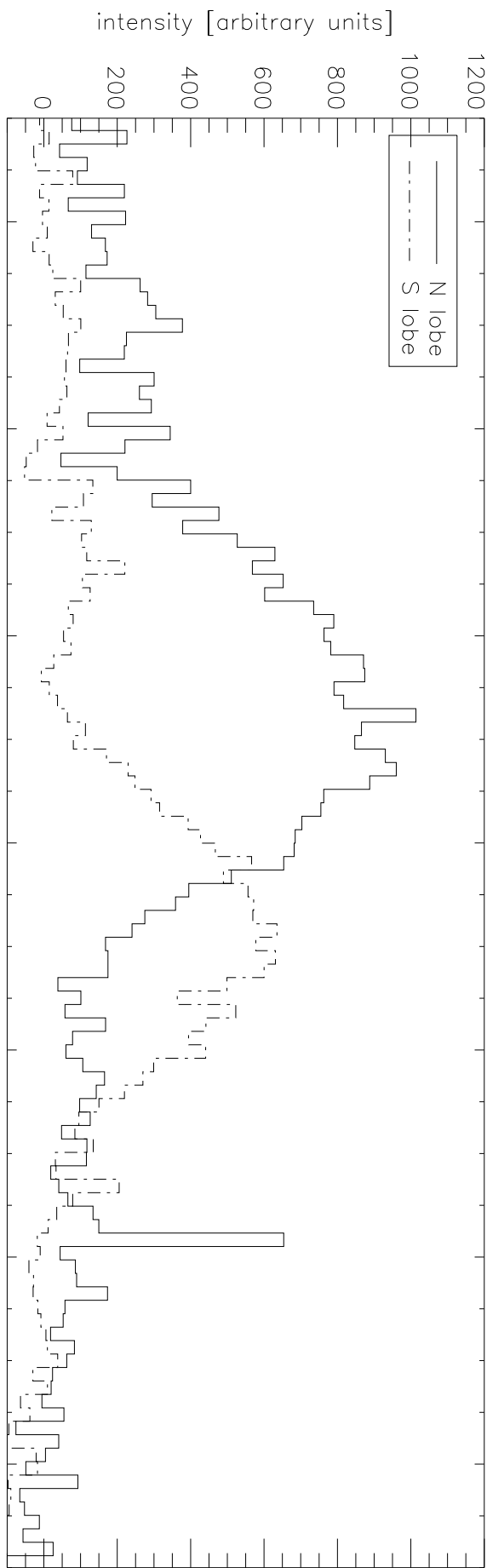
7. Spectra extracted from the spectral image of RAFGL 618. Each spectrum is obtained by summing image sections of width  $2''$  in RA at the offset indicated. The velocity scale of each spectrum is centered on the systemic velocity of RAFGL 618 with respect to the local standard of rest ( $-21 \text{ km s}^{-1}$ ; e.g., Meixner et al. 1998).
8. Comparison of observed and model  $\text{H}_2$  velocity fields for RAFGL 2688. The observed velocity field (left) consists of velocity centroids calculated from the Phoenix data cube. In the model (right), we set the equatorial expansion velocity at  $v_e = 5 \text{ km s}^{-1}$  and the equatorial rotation velocity at  $v_r = 10 \text{ km s}^{-1}$  (see §4.3). We display only those portions of the model velocity image for which the SNR in the HST/NICMOS  $\text{H}_2$  image exceeds  $\sim 5$ , and only those portions of the observed velocity centroid image for which the SNR in the velocity-integrated Phoenix  $\text{H}_2$  image exceeds  $\sim 3$ .

AFGL 2688: NICMOS 2.12 micron  $H_2$

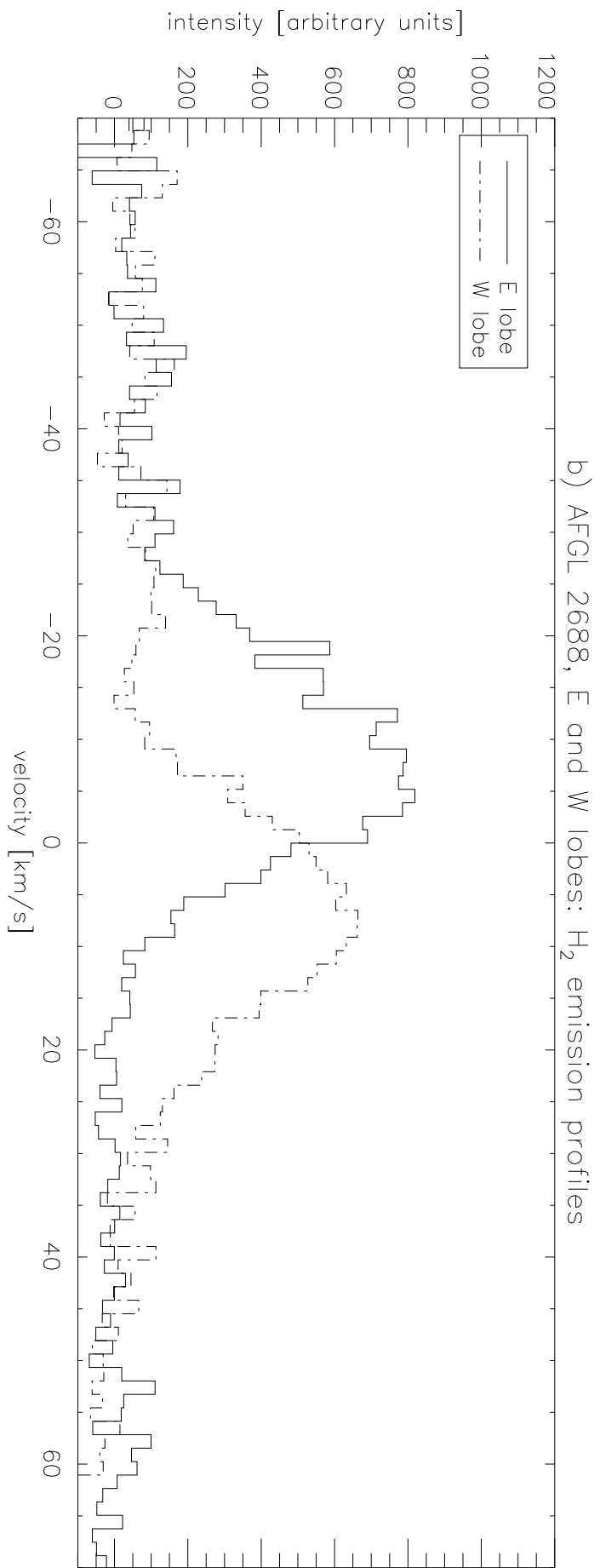


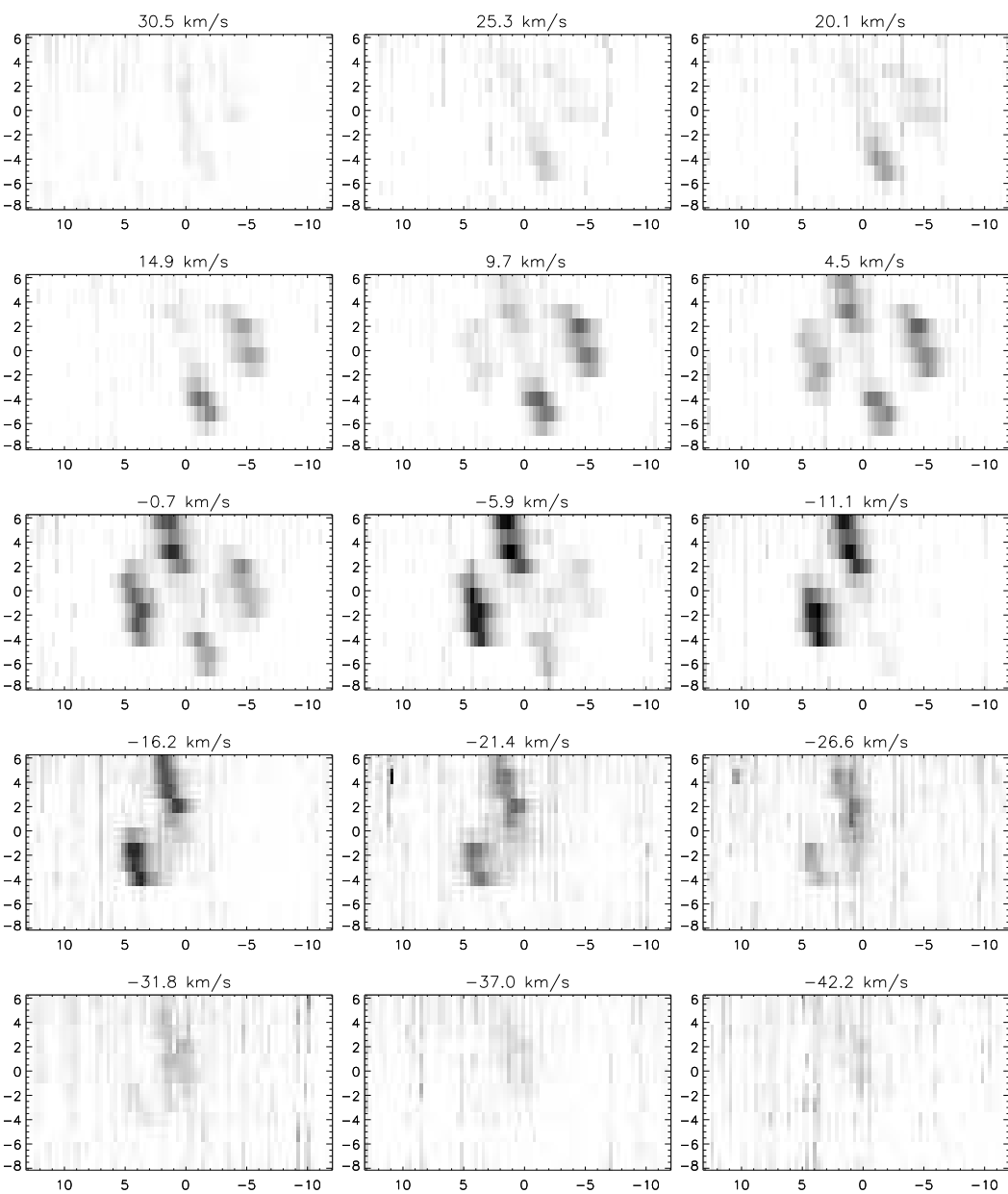


a) AFGL 2688, N and S lobes:  $\text{H}_2$  emission profiles

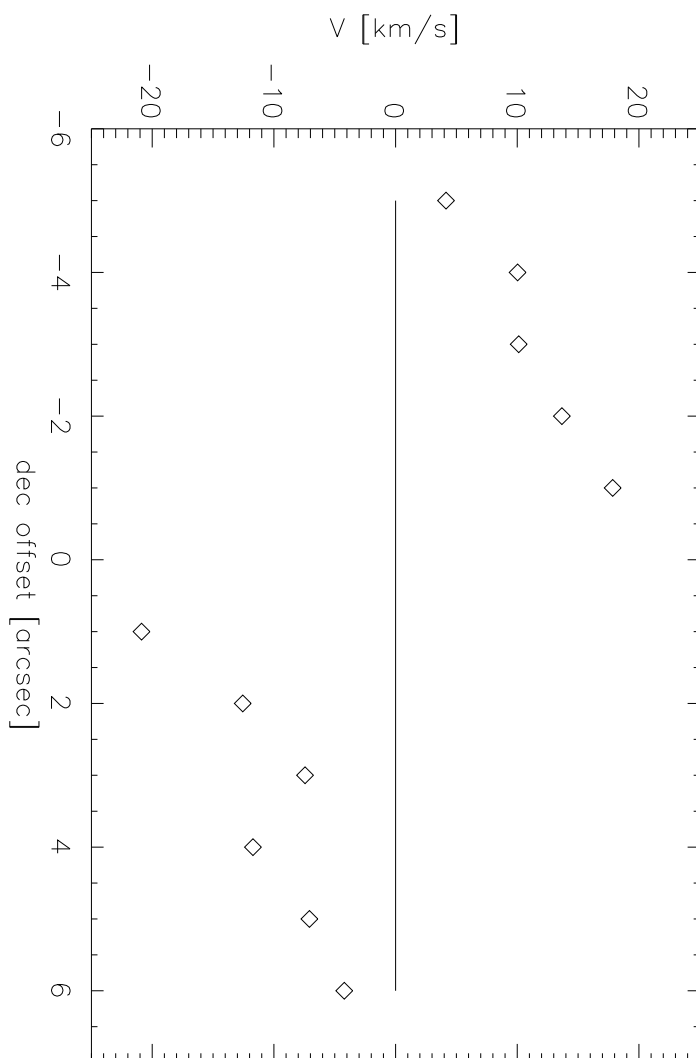


b) AFGL 2688, E and W lobes:  $\text{H}_2$  emission profiles





AFGL 2688:  $\text{H}_2$  line centroid velocities in polar lobes



## AFGL 618, E lobe: H<sub>2</sub> emission profiles

